

# A Graph Attention Spatio-temporal Convolutional Networks for 3D Human Pose Estimation in Video

Junfa Liu, Zhijun Liang, Yihui Li, Yisheng Guan <sup>\*</sup>, and Juan Rojas<sup>[0000-0002-6552-4572]</sup>

Guangdong University of Technology, Guangzhou, China

**Abstract.** 3D pose estimation in video benefits from both temporal and spatial information. Spatiotemporal information can help tackle occlusion and depth ambiguities, which are outstanding problems. Previous methods focused more on time consistency and did not propose an effective way combined with spatial semantics. In this work, we improve the learning of kinematic constraints in the human skeleton; namely posture, 2nd order joint relations, and symmetry. We do this by modeling both local and global spatial information via attention mechanisms. Also, importantly, we carefully design the interleaving of spatial information with temporal information to achieve a synergistic effect. We contribute a simple and effective graph attention spatio-temporal convolutional network (GAST-Net) that comprises of interleaved temporal convolutional and graph attention blocks. Local 2nd order and symmetric constraints can mitigate depth ambiguities for these joints with only one first-order neighbor (like ankle *et al.*), while global posture semantics can more effectively combine time information to address self-occlusion. Experiments on two challenging benchmark datasets, Human3.6M and HumanEva-I, show that we achieve 4.1% and 8.2% improvements.

## 1 Introduction

3D human pose estimation from video has become an active area of research in recent years as it can be used for high-level computer vision tasks like action recognition, virtual reality, and human-robot interaction [1–3]. Previously, 3D pose estimation was computed using depth sensors, motion capture, or multi-view images in indoor environments. However, with recent advances in 2D human pose estimation through deep learning along with massive availability of in-the-wild data there has been great interest in solving 3D pose estimation from monocular images [4–7]. In [5], Pavlakos *et al.* introduced an end-to-end network based on stacked-hourglass networks [8] to predict 3D poses expressed by 3D volume with per-voxel-likelihoods for each joint. Other recent works [9–11] achieved competitive performance and generalization using only 2D representations of human

<sup>\*</sup> Corresponding author. <https://github.com/fabro66/GAST-Net-3DPoseEstimation>

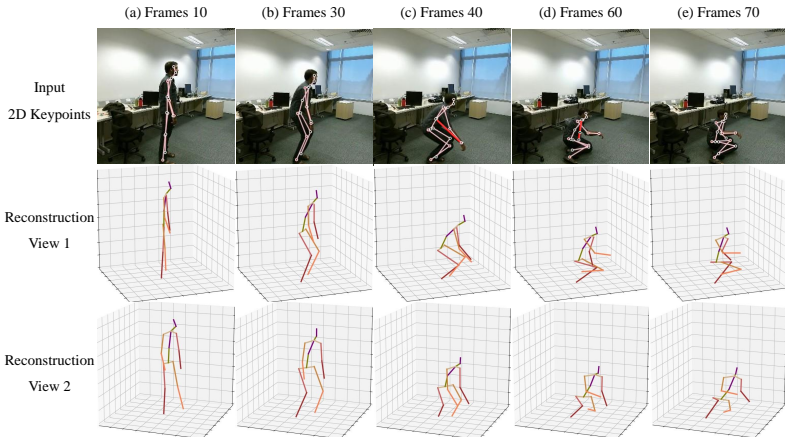


**Fig. 1.** Reconstruction example under the case of depth ambiguities, self-occlusion, and biased 2D poses. The first row shows 2D pose estimation results, where red is the prediction with errors. The second and third rows convey the reconstruction at two different perspectives for better viewing.

poses to avoid the influence of background noise and human external appearance. Nonetheless, estimating 3D poses from 2D keypoints remains an ill-posed problem due to a number of challenges: (i) given that different 3D poses can be mapped to the same 2D pose, there is a depth ambiguity (see Fig. 1 (a)); (ii) self-occlusions occur when humans adopt certain poses (see Fig. 1 (a-e)); and (iii) the input 2D pose may suffer from prediction errors as shown in Fig. 1 (c,d).

To address these problems, recent work has included spatial information from the human skeleton [10, 12–15]. Geometric constraints, including joint symmetry and bone length ratio, were considered by Zhou *et al.* [12] within the loss function. Others, encoded kinematic relations to infer likely poses [6, 13, 16]. Furthermore, with the advent of graph convolutional networks [17–19], Zhao *et al.* [14] represented 2D poses through graphs, whereby joints were modeled as nodes and joint links as edges. Even so, depth ambiguity still remains difficult to solve as well as jittery motions in estimated video.

Temporal modeling has used joint-coordinated vectors in sequence-to-sequence models to tackle these problems [20, 21]. However, the vector representation of joint sequences lacks expressivity for spatial relations. Consider Cai *et al.* work [22], here researchers used a spatio-temporal model for 3D pose estimation. However, the homogeneous manner in which the spatio-temporal data was treated did not allow for the independent treatment of both types of data, which causes cannot effectively capture long-term information. Another important limitation of this work was that it only considered local spatial information but ignored global semantics.

It is clear that additional contextual cues coming from the hierarchical structure of 2D keypoint sequences and posture semantics are critical to resolve depth ambiguities and mitigate occlusions. Occluded joints can be identified through

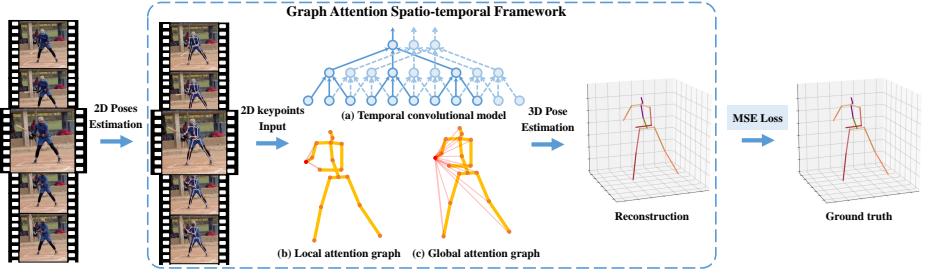


**Fig. 2.** Schematic overview of the GAST-Net framework. The input consists of consecutive 2D pose estimates from RGB images and the output is a sequence of reconstructed 3D poses from the corresponding 2D keypoints. Our GAST-Net architecture includes three components: they synergistic interleaving of (a) a dilated temporal convolutional model (with 2D keypoint sequences as input (bottom) and 3D pose estimates as output (top)) with (b) a set of local attention mechanisms for visualized joints (*i.e.* the right-wrist) including 2nd-order dependencies and symmetric relations. Additionally, we have (c) a global attention mechanism that informs about posture semantics.

local connectivity and the symmetry of joints. Joint location is also improved when we consider global spatial information by decoupling approximate bone ratios and computing the dynamic trajectory of the joints [23, 24]. Additionally, temporal information can be used to smoothen motion.

These findings inspire us to study richer spatio-temporal representations that better mitigate depth ambiguities, occlusion complications, and jitter. To this end, we contribute an interleaved graph-attention spatio-temporal network that further improves the learning related to different constraints in the human kinematics over time. Namely; the learning of joint symmetries, 2nd order relations in distal joints, and global joint semantics that affect posture. The spatial information is then carefully interleaved with the temporal model (we treat both spatial and temporal independently) to synergistically leverage their inference. Our models are both simple to interpret and visualize via skeleton graph.

With regards to temporal modeling, we base our design on the dilated temporal convolutions of [21]. These temporal convolutions can effectively capture long-term information and work with causal convolutions to achieve real-time pose estimation (see Fig. 2 (a)). Local spatial features from joint connections and symmetries are modeled via Graph Convolution Networks (GCNs) and referred to as “Local Attention Graph’s” in our system (see Fig. 2 (b)). As opposed to [22], we design learnable local 2nd order and symmetrical GCNs based on spatial dependencies, rather empirically-derived spatial strategies. For global spatial features, we draw inspiration from [25] and leverage graph attention networks [26] to express posture semantics with data-driven learning. These blocks are referred to as “Global Attention Graph’s” and depicted in Fig. 2 (c). The graph attention block effectively express the hierarchical symmetrical structure of the human body and adaptively extract global semantic information over times. Additionally, local- and global-spatial blocks are interleaved with tempo-

ral blocks to effectively extract and fuse spatio-temporal features of 2D keypoint sequences as shown in Fig. 3 (a).

Experiments on the Human3.6M and the HumanEva-I datasets show that our networks achieve state-of-the-art results in video pose estimation. Additionally, qualitative results show that even when 2D detected keypoints are deviated due to joint occlusion, our model can generate valid 3D poses based on adjacent frames. Furthermore, we learn that through the visualization of the attention on the joints, global attention can learn the strength of the correlation across joints and induce changes according to different postures (see supplementary materials). Our results highlight the power of the proposed local and global graph attention additions as part of an interleaved temporal network to better extract and fuse spatial information over time.

## 2 Related Work

In this section, we first present 3D pose estimation work from 2D pose input and video input; and finish by covering Graph Convolutional Networks (GCNs).

**2D-to-3D Pose:** Since Martinez *et al.* [9] proposed a simple and effective linear layer to lift 2D joint locations to 3D positions, recent works [10, 11, 15, 16, 27, 28] have sought to generate accurate 3D pose estimation from underlying 2D keypoints. Wang *et al.* [11], proposed a semi-supervised approach to solve overfitting by projecting a generated 3D pose back to the 2D image and comparing it with the ground truth. Wang *et al.* [27], designed a novel stereo network with a geometric search scheme to generate a high quality 3D pose in the wild without the need of indoor 3D input. However, 2D joints predicted from 2D detectors inevitably have errors caused by occlusions. In order to generate a valid 3D structure different heuristics have been used. Fang *et al.* [16] imposed a prior to regulate the spatial configuration, while Ci *et al.* [15] used a structured graph to encode the connection relationship between joints. While aiding in reducing errors from occlusions, these methods still suffer from inaccuracies caused by depth ambiguities.

**Video Pose Estimation** As generating accurate 3D poses from a single image is an ill-posed problem, many approaches [10, 20–22, 29–31] exploited temporal information to obtain more robust and smooth 3D poses. Lin *et al.* [31] introduced a multi-stage sequential refined network to predict 3D human pose by using the 2D and 3D poses of the previous stage and frame. A few methods [20, 21] deal with 3D pose estimation as a sequence-to-sequence task. For example, Hossain *et al.* [20] propose a 2-layered normalized LSTM network with residual connections. The latter first encodes 2D pose into a fixed feature vector and then decodes it to a 3D pose. Other recent works incorporate spatial configuration constraints and temporal information to estimate the 3D pose [10, 22]. Cai *et al.* [22] defined the sequence of skeletal joints as a spatio-temporal graph. Cheng *et al.* [30]

combined various features from previous papers to solve the occlusion problem, including filtering out occluded joints, pose regularization, adversarial learning, and data augmentation. Nonetheless, these approaches either do not yet consider spatio-temporal information comprehensively, or are too complicated. We propose a novel and effective end-to-end trained network that interleaves temporal information with learned joint relations in local and global spatial nets.

**Graph Convolutional Networks** GCNs generalize convolutions to graph-structured data. GCNs are roughly classified in two categories: spectral-based and spatial-based [17, 19, 26, 32–35]. Spatial-based GCN are more relevant to our work. Many approaches designed special filters according to varying graph structures to aggregate features [14, 17, 26, 35]. Kipf *et al.* [17] introduced a first-order approximation of spectral filters. Zhao *et al.* [14] extended existing GCNs [17] to Semantic Graph Convolutional Networks which learn unique weights for different neighbors. Velivckovic *et al.* [36] proposed Graph Attention Networks, which directly computes the weight relation between a central node and its first-order neighbors through attention mechanism. Our spatial network uses both GCNs proposed by [14] and [36] to obtain local and global features of each joint.

### 3 Graph Attention Spatio-Temporal Networks

Given a sequence of 2D pose predictions from videos, our goal is to output a sequence of 3D coordinates based on a root joint—the pelvis. We present an attention-based spatio-temporal network that makes full use of spatio-temporal information and addresses the problems of self-occlusion in poses and depth ambiguities. We understand spatial and temporal data to be heterogeneous. As such we treat them independently but interleave them in a synergistic manner allowing us to leverage the benefits of TCNs. Our spatial blocks aim to effectively model the symmetrical hierarchy of the human body as well as the kinematic joint constraints via novel convolutional kernels at the local and global levels. Furthermore, we exploit attention mechanisms to learn specific inter-joint relations that are easily interpretable, visualizable, and that can be trained end-to-end in a straight-forward fashion.

To this end, we introduce our interleaved graph attention spatio-temporal network. The temporal component is designed from dilated TCNs to tackle long-term patterns (Sec. 3.1). As for the spatial components, we have a local spatial attention network designed from GCNs and a global attention network designed from GATs. These GNNs, both use novel convolutional kernels that model the hierarchical and symmetrical structure of the human skeleton. The kernels adaptively extract global semantic information to better encode the human body’s spatial characteristics. Fig. 3 (a) depicts an instantiation of the proposed framework with a receptive field size of 27 frames, whilst Fig. 3 (b) depicts the graph attention block which is composed of global and local spatial blocks. Note that according to the network characteristics of TCNs, our proposed model can train under varying numbers of long-sequence receptive fields as needed.

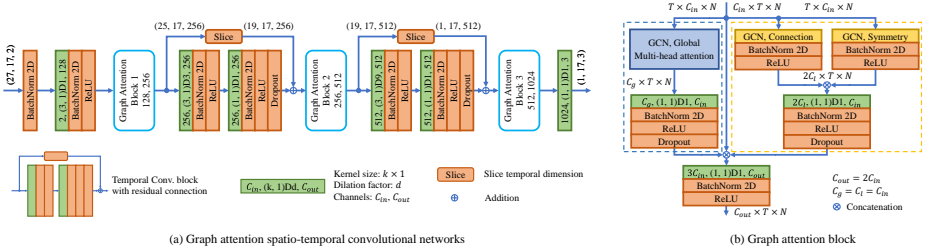


**Fig. 3.** (a) An instantiation of GAST-Net for 3D pose estimation. The GAST-Net consists of 2 Temporal Convolution Blocks and 3 Graph Attention Blocks. Given a 2D pose sequence, the output is a sample 1-frame prediction. Dimensions are enclosed in parenthesis, *e.g.* (27, 17, 2), which denotes 27 frames, 17 joints, and 2 channels. (b) The architecture of graph attention block. The yellow dotted box indicates the graph local attention layer, while the blue dotted box indicates global graph attention layer. By concatenation operation and following a 2D convolution layer, it outputs spatio-temporal features.

### 3.1 Temporal Convolutional Network

The temporal dilated convolutional model [21] consists of an input layer, an output layer and  $B$  temporal convolutional blocks that flexibly control the receptive field by setting the kernel size and the dilation factor of the convolution. Each block first performs a 1D convolution with kernel size  $k$  and dilation factor  $d = k^B$ , followed by a convolution with kernel size 1. The main difference compared to [21] is that we represent the input 2D pose sequence as a three-dimensional vector  $(C, T, N)$ , where  $C$  is the number of coordinate dimensions  $(x, y)$ ,  $T$  is the number of receptive fields, and  $N$  is the number of joints in each frame. To save the spatial information across time steps, we replace the original 1D convolution with 2D convolutions for a kernel size of  $k \times 1$ . Simultaneously, each batch normalization [37] is changed to 2D, and it is added at the beginning to normalize the input data. The dropout [38] is only employed at the second convolution layer of blocks to improve generalization. Fig. 2 shows an instantiation of GAST-Net for a receptive field size of 27 frames with  $B = 2$  blocks.

### 3.2 Local Attention Graph.

At any given frame in time, 2D keypoints represent the joints of the human skeleton. The skeleton is naturally represented by an undirected graph with joints as nodes and human-links as edges. GCNs uses graphs to model spatial configuration that influences 3D pose estimation and action recognition. Previous GCN methods [2, 22, 39] have used weight-sharing matrices or empirically-derived spatial strategies—that are fixed by nature—to construct connections between joints. Our work differs in that our GCN learns individual weights between joint pairs.

In this work, we construct the skeleton graph of 2D keypoints in a frame based on the SemGCN proposed by Zhao [14]. More concretely, we define a 2D

pose (within a frame) as a graph  $\mathcal{G} = (\mathcal{V}, \mathcal{E})$ , where  $\mathcal{V}$  is the set of  $N$  nodes and  $\mathcal{E}$  edges.  $X = \{x_1, x_2, \dots, x_N \mid x_i \in \mathbb{R}^{1 \times C}\}$  is the set of node features with  $C$  channels. The structure of the graph can be initialized by a first-order adjacency matrix  $A \in \mathbb{R}^{N \times N}$  that indicates the existing connections between joints and an identity matrix  $I$  indicating self-connections.  $\tilde{A} = (A + I)$  expresses the convolutional kernel in GCNs. According to the definition of SemGCN, given the node features of the  $l$ -th layer, the output features of the subsequent layer are obtained through the following convolution:

$$X^{(l+1)} = \rho(M \odot \tilde{A})X^{(l)}W \quad (1)$$

where  $W \in \mathbb{R}^{C_l \times C_{l+1}}$  is a learnable matrix used to transform output channels,  $M \in \mathbb{R}^{N \times N}$  is a learnable mask matrix,  $\odot$  is an element-wise multiplication operation, and  $\rho$  is a Softmax nonlinearity that normalizes the contribution of the features of a node to a corresponding neighboring node in a graph. By introducing a set of mask matrix  $M_c \in \mathbb{R}^{N \times N}$  for the channels of the output node features, Eqtn. 1 can be extended to:

$$X^{(l+1)} = \parallel_{c=1}^{C_{l+1}} \rho(M_c \odot \tilde{A})X^{(l)}w_c \quad (2)$$

where  $\parallel$  denotes a channel-wise concatenation and  $w_c$  is the  $c$ -th row of matrix  $W$ .

Eqtn. 2 jointly learns the unique semantics across neighboring nodes. However, and very notably, this first-order neighbor representation poorly models (i) the symmetrical structure of a torso-centered human body and (ii) kinematic constraints in the human body. Thus, we propose that the structural knowledge existent in symmetry is explicitly considered. Furthermore, another reason why first-order neighbor representations struggle to model human spatial relations is that joint constraints are confined to first-order neighboring joints. More precisely, these joints (*i.e.* wrist, ankle, and head) at the end of the human kinematic chain has only one first-order neighboring joint, so their position in space cannot be effectively located by the first-order neighborhood. Such joints are also the largest source of modeling errors [6, 20]. But we can exploit the relationship of the entire kinematic chain (*i.e.* ankle-knee-hip, wrist-elbow-shoulder, and head-neck-throat) to mitigate the location ambiguity.

Based on the aforementioned limitations, we design two novel convolution kernels: (i) a symmetric matrix  $\tilde{A}_s$  that encodes the human skeleton symmetrical structure for joints that have a symmetrical counterpart (*i.e.* limb joints). (ii) an adjacency matrix  $\tilde{A}_c$  that explicitly encodes first- and second-order connections for distal joints (*i.e.* ankle-knee, ankle-hip). The rest of the nodes are only modeled through first-order connections<sup>1</sup>.

Note that each of these two convolution kernels are applied to two distinct GCNs; where each GCNs is followed by batch normalization [37] and rectified linear units [40] as shown in the yellow dotted box of Fig. 3 (b).

<sup>1</sup> In the future, we will consider automatically learning these relationships



### 3.3 Global Attention Graph.

Disconnected joints (*i.e.* wrist-ankle or wrist-head) are an important consideration in a global analysis. The human skeleton’s kinematic chain entails that joints far away from each other can affect each other and aid in more effectively defining constraints (think sitting down or running). As such disconnected joints can play an important role in addressing depth ambiguities and occlusions. In order to adaptively and effectively encode non-local relationships among joints, we propose a global GCN with a multi-head attention mechanism that extends the existing mechanism of Eqtn. 2 from first-order relationships to global relationships (it also operates end-to-end):

$$X^{(l+1)} = \parallel_{k=1}^K (B_k + C_k) X^{(l)} W_k \quad (3)$$

where,  $K$  is the number of attention heads,  $B_k \in \mathbb{R}^{N \times N}$  is a learnable global adjacency matrix,  $C_k \in \mathbb{R}^{N \times N}$  is an adaptive adjacency matrix, and  $W_k \in \mathbb{R}^{C_l \times (C_l/K)}$  is a transformed matrix. In this work we employ  $K = 4$  parallel attention heads. Next, we discuss the redefined adjacency matrix  $B_k$  and  $C_k$  in detail.

$B_k$  expresses a data-dependent matrix which learns a unique graph for each node. We adopt the attention coefficient function proposed by [36] to determine whether a connection exists between nodes and how strong the connection is. That is, given two node features  $x_i$  and  $x_j$ , we first apply two embedding functions  $\theta$  and  $\phi$  to downsample the features of each node from  $C_l$  to  $C_l/K$  channels. Since the number of channels for each node is reduced, the total computational cost for multi-attention is similar to that of single-headed attention with full channels. Downsampling features will lose some information, but this is based on the consideration of flexibly expressing joint relationships while avoiding increasing computational complexity. Then we concatenate the two embedded features, and compute their dot product with a weight vector  $w_f$  to produce a scalar output. To facilitate coefficient comparisons across nodes, the scalar outputs are normalized by the softmax function. The operation is presented in Eqtn. 4:

$$\alpha_{ij} = \frac{\exp(\sigma(w_f[\theta(x_i) \parallel \phi(x_j)]))}{\sum_{k=1}^N \exp(\sigma(w_f[\theta(x_i) \parallel \phi(x_k)]))} \quad (4)$$

where  $\theta$  and  $\phi$  is a convolution with the kernel size of 1,  $[\cdot \parallel \cdot]$  denotes concatenation, and  $\sigma$  denotes LeakyReLU nonlinearity with negative input slope  $\alpha = 0.2$ .

$C_k$  is an adaptive learnable adjacency matrix, inspired by [25], with an initialization value of zero. The value of  $C_k$  is not limited to special node features like  $B_k$ , which is updated during the training process. The elements of  $C_k$  are arbitrary.

### 3.4 Graph Attention Block.

The overall architecture of the graph attention block is shown in Fig. 3 (b). The block optimizes the spatio-temporal embedding by concatenating the incoming



temporal features with the local and global spatial features based on channel dimensionality. The output features are finally fused through a 2D convolutional layer. The block then allows the local attention layer to focus on information stemming from joint connections and symmetry, whilst the global attention layers learns posture semantics.

## 4 Experiments

**Datasets.** We evaluate our algorithms on two publicly available datasets: Human3.6M and HumanEva-I. Human3.6M captures data through four synchronized cameras at 50 Hz and contains 3.6 million video frames with 11 professional subjects performing 15 daily activities (*i.e.* walking and sitting). The dataset provides 2D and 3D joint locations for each corresponding image. Following previous methods [9, 15, 20, 21], we employ subjects 1, 5, 6, 7 and 8 for training and subjects 9 and 10 for testing. HumanEva-I, is a much smaller dataset and captures data through three camera views at 60 Hz. Following [20, 21], the time-series data from three actions (walk, jog, box) is split between training and testing.

**Protocols** We use two common evaluation protocols in our experiments. Protocol #1 calculates the mean per joint positioning error (MPJPE) between the ground truth and the predicted 3D coordinates across all cameras and joints. Protocol #2 employs a rigid alignment (Procrustes analysis) with the ground truth before calculating the mean per joint positioning error (P-MPJPE).

**Implementation Details** We trained our networks with receptive fields of sizes 9, 27, 81 and 243 to verify the effectiveness of our model architecture. To make the model lightweight, for networks with receptive fields of 9 and 27, we increase the number of output channels of the first dilated convolutional layer to 128, while the network with 81 and 243 receptive fields is set to 64 and 32 channels respectively. Note that our loss function only computes the MPJPE between the predicted 3D location and ground truth without using any tricks (*i.e.* constraint).

Like [21], we use Mask-RCNN [41] with a ResNet-101-FPN backbone as the human bounding box detector and CPN (extended from FPN) [42] is used to estimate the 2D keypoints. Both Mask-RCNN and CPN are pre-trained on the COCO dataset and then fine-tuned on the Human3.6M dataset. Since 3D joints provided by each dataset are different, we predict a 17-joint skeleton on Human3.6M and a 15-joint skeleton on HumanEva-I. We downsample the Human3.6M dataset from 50 FPS to 10 FPS. High frame rates have a redundancy that negatively affects the encoding of global semantics over time. On the other hand, as the duration of each video in the HumanEva-I dataset is too short, no downsampling is performed. Since too long duration is not suitable for real-time estimation, we also don't perform downsampling for 243 receptive field model. We adopt horizontal flip augmentation at train and test time.

We implement our method with the PyTorch framework and train end-to-end. For Human3.6M, we optimize with Amsgrad with a mini-batch size of  $b =$

**Table 1.** Ablation study on the effectiveness of different components in GAST-Net on Human3.6M under protocol # 1.

Method	Error (mm)	$\Delta$	# Parameters
Ours w/o Local connection GCNs	47.6	1.4	5.83M
Ours w/o Local symmetry GCNs	47.4	1.2	5.86M
Ours w/o Global GCNs of $B_k$	52.3	6.1	6.92M
Ours w/o Global GCNs of $C_k$	47.3	1.1	6.84M
Ours w/o Train augmentation	47.6	1.4	6.92M
Ours w/o Test augmentation	46.7	0.5	6.92M
Ours w/ Causal convolution	47.1	0.9	6.92M
Ours (GAST-Net)	46.2	-	6.92M

128, and train for 60 epochs. The learning rate starts at 0.001 and then applies a learning shrink factor  $\alpha = 0.95$  in each epoch. The dropout rate  $p$  in each dropout layer is set to 0.05. For HumanEva-I, we use  $b = 32$ ,  $\alpha = 0.98$ ,  $p = 0.5$ , and train for 200 epochs.

To train the dilated convolutional model, we use Pavlo’s optimized training strategy for single-frame predictions instead of the layer-by-layer implementation [21]. For single-frame scenarios, dilated convolutions are known to waste a large number of computations. To reduce the inefficiency, dilated convolutions are replaced with strided convolutions. At inference, we switch and consider the the entire video sequence. We change from the optimized training strategy to the layer-by-layer implementation to make faster predictions. As in [21], both symmetric (our default) and causal convolutions can be used to output the 3D pose. The symmetric format outputs the 3D pose from the intermediate frames in the video sequences. The causal format uses the last frame and is the preferred one for real-time requirements. Their effectiveness are discussed in the ablation studies in Sec. 4.1.

## 4.1 Ablation Studies

To assess the effect of each component in our model, we perform an ablation analysis for our 27 receptive fields model on Human3.6M under Protocol #1. Specifically, we remove different GCNs including: local connections, symmetry,  $B_k$ ,  $C_k$ , as well as training and testing without augmentation, and using causal convolutions for 3D output estimation. The results are summarized in Table 1.

The biggest contributor to the accuracy of our system is the global GCN  $B_k$ . The result validates our hypothesis that global semantics effectively construct joint constraints that more closely reconstruct the true human kinematics. Other components affect the system as follows: The global spatial adaptive matrix  $C_k$  reduces error by 1.1mm. Removing the local spatial GCNs for local connections and symmetry increase error by 1.4mm and 1.2mm respectively. This result indicates that these two local spatial configurations are also important for better pose estimation. Horizon flip augmentation reduces error by 1.4mm during training and 0.5mm during test. Finally, symmetrical convolutions outperformed causal convolutions for real-time prediction.

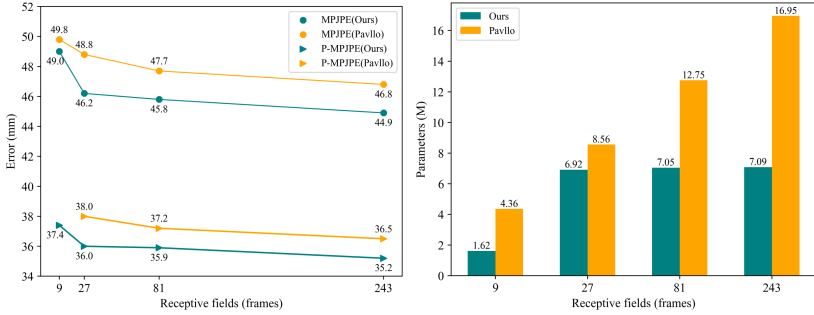


**Fig. 4. Left:** Comparison with TCNs [21] in different receptive fields on Human3.6M under protocol #1 and #2. **Right:** Comparison with the parameters of model.

## 4.2 Comparison with TCNs

Fig.4 compares the number of parameters and the 3D pose estimation errors between TCNs [21] and our four receptive field models. As can be seen on the left of Fig.4, we obtain smaller estimation errors for all receptive field combinations on Human3.6M under both protocols. In particular, our model with 27 receptive fields is also slightly better than the TCNs with 243 receptive fields, which shows that the use of spatial information significantly contributes to reconstructing more accurate 3D pose estimates. For the right side of Fig.4, we see that our model uses 37.1%, 80.8%, 55.3%, and 41.8% fewer parameters compared to the TCNs’ 9, 27, 81, and 243 receptive field models respectively. We believe the superior performance of our model with fewer parameters is explained by the better modelling capability of the spatial modules.

## 4.3 Comparison with State-of-the-Art.

**Evaluation on Human3.6M.** Table 2 shows the performance of our three (27, 81, 243) receptive field models compared to previous state-of-the-art results on Human3.6M. We also indicate whether these compared methods have exploited temporal or spatial information. Note that we only compared the method of 2D-to-3D pose [9, 10, 15, 16, 20–22, 29]. As shown in the table, we achieve the lowest average error on the two protocols for all SOTA results. Moreover, compared with SOTA, our method yields lower errors across most actions. In particular, the “sitting down” (SitD) action, where one sees the most self-occlusions, was where our algorithm fared the best.

Table 3 evaluates our model based on ground truth 2D poses. We outperform both the baseline [9] and SOTA [21] by a large margin on both protocols. More specifically, by using our results for 81 receptive fields (our best average performance) the mean error is reduced by 4.7 mm (12.6%) on protocol # 1 and by 2.7 mm (9.9%) on protocol # 2 with fewer parameters. As before, we speculate the improvement is due to the more effective encoding of spatial features given accurate 2D poses. Furthermore, we examine the performance of our architecture with other 2D keypoint detectors. In particular, we examine the stacked

**Table 2.** Quantitative comparisons of MPJPE in millimeters between the estimated pose and the ground-truth on the Human3.6M under Protocol #1 and Protocol #2. T denotes the number of receptive fields, (†) indicates the use of spatial information and \* expresses the use of causal convolution. Best in bold, second best underlined.

Protocol #1	Dir.	Disc.	Eat	Greet	Phone	Photo	Pose	Purch.	Sit	SitD.	Smoke	Wait	WalkD.	Walk	WalkT.	Avg
Martinez [9], ICCV17 (T=1)	51.8	56.2	58.1	59.0	69.5	78.4	55.2	58.1	74.0	94.6	62.3	59.1	65.1	49.5	52.4	62.9
Fang [16], AAAI18 (T=1)(†)	50.1	54.3	57.0	57.1	66.6	73.3	53.4	55.7	72.8	88.6	60.3	57.7	62.7	47.5	50.6	60.4
Lee [29], ECCV18 (T=3)(†)	<b>40.2</b>	49.2	47.8	52.6	50.1	75.0	50.2	43.0	55.8	73.9	54.1	55.6	58.2	43.3	43.3	52.8
Hossain [20], ECCV18 (T=5)	44.2	46.7	52.3	49.3	59.9	59.4	47.5	46.2	59.9	65.6	55.8	50.4	52.3	43.5	45.1	51.9
Dabral [10], ECCV18 (T=20)(†)	44.8	50.4	44.7	49.0	52.9	61.4	<u>43.5</u>	45.5	63.1	87.3	51.7	48.5	52.2	37.6	41.9	52.1
Ci [15], ICCV19 (T=1)(†)	46.8	52.3	44.7	50.4	52.9	68.9	49.6	46.4	60.2	78.9	51.2	50.0	54.8	40.4	43.3	52.7
Cai [22], ICCV19 (T=7)(†)	44.6	47.4	45.6	48.8	50.8	59.0	47.2	43.9	57.9	61.9	49.7	46.6	51.3	37.1	39.4	48.8
Pavlo [21], CVPR19 (T=243)*	45.9	48.5	44.3	47.8	51.9	57.8	46.2	45.6	59.9	68.5	50.6	46.4	51.0	34.5	35.4	49.0
Pavlo [21], CVPR19 (T=243)	45.2	46.7	43.3	45.6	48.1	55.1	44.6	44.3	57.3	65.8	47.1	44.0	49.0	32.8	33.9	46.8
ours, (T=27)(†)	44.9	46.7	41.9	45.6	47.9	56.1	44.2	45.5	57.1	59.1	46.8	43.5	47.5	32.6	33.1	46.2
ours, (T=81)(†)	45.5	<b>44.9</b>	42.1	45.8	47.4	<u>54.4</u>	<b>43.1</b>	43.7	58.1	60.0	47.2	43.8	<b>46.6</b>	<u>31.5</u>	<u>31.9</u>	45.7
ours, (T=243)(†)*	45.5	48.4	43.9	48.3	49.3	57.6	45.0	45.8	57.3	61.4	49.3	45.3	49.6	33.7	33.4	47.7
ours, (T=243)(†)	43.3	46.1	<b>40.9</b>	<b>44.6</b>	<b>46.6</b>	<b>54.0</b>	44.1	<b>42.9</b>	<b>55.3</b>	<b>57.9</b>	<b>45.8</b>	<b>43.4</b>	47.3	<b>30.4</b>	<b>30.3</b>	<b>44.9</b>
Protocol #2	Dir.	Disc.	Eat	Greet	Phone	Photo	Pose	Purch.	Sit	SitD.	Smoke	Wait	WalkD.	Walk	WalkT.	Avg
Martinez [9], ICCV17 (T=1)	39.5	43.2	46.4	47.0	51.0	56.0	41.4	40.6	56.5	69.4	49.2	45.0	49.5	38.0	43.1	47.7
Fang [16], AAAI18 (T=1)(†)	38.2	41.7	43.7	44.9	48.5	55.3	40.2	38.2	54.5	64.4	47.2	44.3	47.3	36.7	41.7	45.7
Lee [29], ECCV18 (T=3)(†)	34.9	35.2	43.2	42.6	46.2	55.0	37.6	38.8	50.9	67.3	48.9	35.2	31.0	50.7	34.6	43.4
Hossain [20], ECCV18 (T=5)	36.9	37.9	42.8	40.3	46.8	46.7	37.7	36.5	48.9	52.6	45.6	39.6	43.5	35.2	38.5	42.0
Dabral [10], ECCV18 (T=20)(†)	<b>28.0</b>	<b>30.7</b>	39.1	<b>34.4</b>	37.1	44.8	<b>28.9</b>	<b>31.2</b>	<b>39.3</b>	60.6	39.3	<b>31.1</b>	37.8	25.3	28.4	36.3
Ci [15], ICCV19 (T=1)(†)	36.9	41.6	38.0	41.0	41.9	51.1	38.2	37.6	49.1	62.1	43.1	39.9	43.5	32.2	37.0	42.2
Cai [22], ICCV19 (T=7)(†)	35.7	37.8	36.9	40.7	39.6	45.2	37.4	34.5	46.9	50.1	40.5	36.1	41.0	29.6	33.2	39.0
Pavlo [21], CVPR19 (T=243)*	35.1	37.7	36.1	38.8	38.5	44.7	35.4	34.7	46.7	53.9	39.6	35.4	39.4	27.3	28.6	38.1
Pavlo [21], CVPR19 (T=243)	34.1	36.1	34.4	37.2	36.4	42.2	34.4	33.6	45.0	52.5	37.4	33.8	37.8	25.6	27.3	36.5
ours, (T=27)(†)	34.0	36.6	33.5	37.2	36.4	42.7	34.1	34.4	45.5	47.0	37.2	<b>33.0</b>	36.6	24.9	26.9	36.0
ours, (T=81)(†)	33.9	36.0	33.9	37.1	36.7	42.6	33.7	33.0	46.0	47.1	37.6	33.5	35.9	25.0	26.0	35.9
ours, (T=243)(†)*	34.9	37.5	34.9	38.3	37.4	44.0	34.4	34.6	45.1	48.0	49.3	34.8	37.7	26.2	27.1	36.9
ours, (T=243)(†)	32.7	36.2	<b>33.4</b>	36.5	<b>36.0</b>	<b>41.5</b>	33.6	33.1	44.1	<b>46.8</b>	<b>36.7</b>	33.1	<b>35.8</b>	<b>24.2</b>	<b>24.8</b>	<b>35.2</b>

**Table 3.** The performance of our method on 2D pose from ground truth and Stacked Hourglass(SH) detector.

Method	Ground Truth		SH Fine-tuned	
	Protocol# 1	Protocol# 2	Protocol# 1	Protocol# 2
Martinez, (T=1)	45.5	37.1	62.9	47.7
Pavlo, (T=243)	37.2	27.2	53.4	<b>40.1</b>
Ours, (T=81)	<b>32.5</b>	<b>24.5</b>	<b>51.9</b>	40.3

hourglass detector [8]. This detector is pre-trained on MPII and fine-tuned on Human3.6M. As we can see from the right-hand-side of Table 3, we also have improvements compared to Pavlo on protocol #1 (2.8% or 1.5mm) and slightly lower performance on protocol #2 (-0.2mm).

**Evaluation on HumanEva-I.** Since videos in HumanEva-I dataset have much smaller durations compared with those in Human3.6M, we choose to use fewer receptive fields—27—for evaluation under protocol# 2. Table 4 shows that we achieved the best results in each action except the S3 of Walking due to corrupted mocap data. Note that for the "Box" action, which entails self-occlusion and fast motion, our error measure is 12.5 mm lower than the next best result. The result indicates that by considering the local and global semantics, as we did, the architecture is able to generate a kinematic model of the human pose that enables better estimates. Furthermore, by having such strong performance of HumanEva-I, it is evident that our architecture generalizes well in small datasets.

**Table 4.** Comparison on HumanEva-I under protocol#2. Best in bold, second best underlined. Note that the high error on S3’s “Walk” is due to corrupted mocap data. Some methods did not report S3 ”Box” results, they are marked ”-”.

Method	Walk			Jog			Box			Avg.
	S1	S2	S3	S1	S2	S3	S1	S2	S3	
Lin [31], CVPR’17	26.5	20.7	38.0	41.0	29.7	33.2	39.4	57.8	61.2	38.6
Pavlakos [5], ICCV’17	22.3	19.5	<u>29.7</u>	28.9	21.9	23.8	-	-	-	-
Martinez [9], ICCV’17	19.7	17.4	46.8	26.9	18.2	18.6	-	-	-	-
Pavlakos [7], CVPR’18	18.8	12.7	<b>29.2</b>	23.5	15.4	14.5	-	-	-	-
Lee [29], ECCV’18	18.6	19.9	30.5	25.7	16.8	17.7	42.8	48.1	53.4	30.4
Pavlo [21], CVPR’19	<u>13.9</u>	<u>10.2</u>	46.6	<u>20.9</u>	<u>13.1</u>	<u>13.8</u>	<u>23.8</u>	<u>33.7</u>	<u>32.0</u>	<u>23.1</u>
Ours	<b>13.7</b>	<b>9.2</b>	46.2	<b>20.1</b>	<b>12.5</b>	<b>12.7</b>	<b>21.8</b>	<b>27.8</b>	<b>27.0</b>	<b>21.2</b>

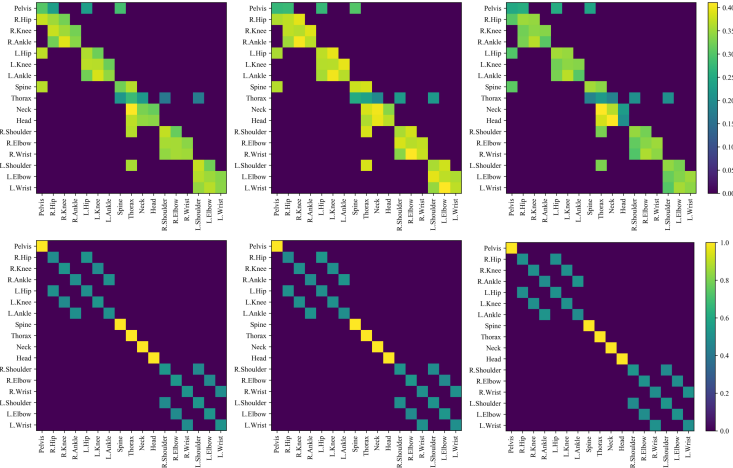


**Fig. 5.** Visualization of local weight matrices for local (1st row) and symmetric (2nd row) GCNs across 3 attention blocks.

**Local Attention Visualization** To better understand the joint relationships both at the local and symmetrical level, we visualize our model’s local weight matrices (under 27 receptive fields). Weight matrices contain the average result across all channels (see Eqtn. 2). Fig. 5 visualizes the local connections in row 1 and the symmetric connections in row 2 across 3 attention blocks of our network. As for the local connections, notice the strong diagonal trend in the joint matrix. This indicates our model learns strong correlations across first and second order neighboring joints. In the second row, the visualization shows how the system learns symmetric joints by producing binary values in which all symmetric joints take on the same valence.

#### 4.4 Qualitative Results.

Fig. 6 is some results estimated by our 27 receptive field model. In the first row shows the reconstruction in two common self-occlusion actions (walking and sitting down). We can observe that even if there are predicted errors in the 2D

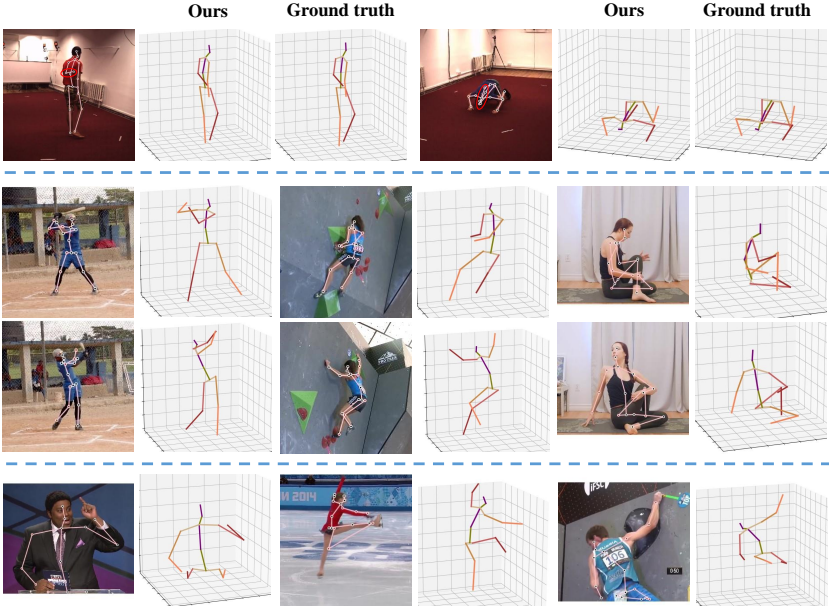


**Fig. 6.** 3D human pose reconstructed from Human3.6 and YouTube videos. The first row shows two self-occlusion cases estimated from Human3.6M. The second and third rows show some good results reconstructed from YouTube video. The last row shows some failure cases caused by long-term heavy occlusion or big 2D detection error.

poses (marked by red circles in figure), our proposed model still can generate an accurate 3D pose via exploiting the temporal consistency and the spatial posture semantics. In the second and third rows show some good reconstruction estimated from YouTube videos. In the last row, there are some failure case caused by long-term heavy occlusion or big 2D prediction error.

## 5 Conclusion

We introduce a graph attention spatio-temporal network for 3D human pose estimation in video. The proposed graph attention block effectively encodes the strength of relationship among joints and interleaves with temporal convolution to flexibly expand receptive fields. Our method can make full use of spatio-temporal information to mitigate depth ambiguities and self-occlusion. We achieved state-of-the-art performance on two benchmark datasets, Human3.6M and HumanEva-I. The qualitative results shows that our model can construct valid 3D structure, even there are certain errors on predicted 2D poses.

## References

1. Zimmermann, C., Welschehold, T., Dornhege, C., Burgard, W., Brox, T.: 3d human pose estimation in rgbd images for robotic task learning. In: 2018 IEEE Interna-

- tional Conference on Robotics and Automation (ICRA), IEEE (2018) 1986–1992
2. Yan, S., Xiong, Y., Lin, D.: Spatial temporal graph convolutional networks for skeleton-based action recognition. In: Thirty-second AAAI conference on artificial intelligence. (2018)
3. Mehta, D., Sridhar, S., Sotnychenko, O., Rhodin, H., Shafiei, M., Seidel, H.P., Xu, W., Casas, D., Theobalt, C.: Vnect: Real-time 3d human pose estimation with a single rgb camera. *ACM Transactions on Graphics (TOG)* **36** (2017) 1–14
4. Yang, W., Ouyang, W., Wang, X., Ren, J., Li, H., Wang, X.: 3d human pose estimation in the wild by adversarial learning. In: Proceedings of the IEEE Conference on Computer Vision and Pattern Recognition. (2018) 5255–5264
5. Pavlakos, G., Zhou, X., Derpanis, K.G., Daniilidis, K.: Coarse-to-fine volumetric prediction for single-image 3d human pose. In: Proceedings of the IEEE Conference on Computer Vision and Pattern Recognition. (2017) 7025–7034
6. Sun, X., Shang, J., Liang, S., Wei, Y.: Compositional human pose regression. In: Proceedings of the IEEE International Conference on Computer Vision. (2017) 2602–2611
7. Pavlakos, G., Zhou, X., Daniilidis, K.: Ordinal depth supervision for 3d human pose estimation. In: Proceedings of the IEEE Conference on Computer Vision and Pattern Recognition. (2018) 7307–7316
8. Newell, A., Yang, K., Deng, J.: Stacked hourglass networks for human pose estimation. In: European conference on computer vision, Springer (2016) 483–499
9. Martinez, J., Hossain, R., Romero, J., Little, J.J.: A simple yet effective baseline for 3d human pose estimation. In: Proceedings of the IEEE International Conference on Computer Vision. (2017) 2640–2649
10. Dabral, R., Mundhada, A., Kusupati, U., Afaq, S., Sharma, A., Jain, A.: Learning 3d human pose from structure and motion. In: Proceedings of the European Conference on Computer Vision (ECCV). (2018) 668–683
11. Wandt, B., Rosenhahn, B.: Repnet: Weakly supervised training of an adversarial reprojection network for 3d human pose estimation. In: Proceedings of the IEEE Conference on Computer Vision and Pattern Recognition. (2019) 7782–7791
12. Zhou, X., Huang, Q., Sun, X., Xue, X., Wei, Y.: Towards 3d human pose estimation in the wild: a weakly-supervised approach. In: Proceedings of the IEEE International Conference on Computer Vision. (2017) 398–407
13. Moreno-Noguer, F.: 3d human pose estimation from a single image via distance matrix regression. In: Proceedings of the IEEE Conference on Computer Vision and Pattern Recognition. (2017) 2823–2832
14. Zhao, L., Peng, X., Tian, Y., Kapadia, M., Metaxas, D.N.: Semantic graph convolutional networks for 3d human pose regression. In: Proceedings of the IEEE Conference on Computer Vision and Pattern Recognition. (2019) 3425–3435
15. Ci, H., Wang, C., Ma, X., Wang, Y.: Optimizing network structure for 3d human pose estimation. In: Proceedings of the IEEE International Conference on Computer Vision. (2019) 2262–2271
16. Fang, H.S., Xu, Y., Wang, W., Liu, X., Zhu, S.C.: Learning pose grammar to encode human body configuration for 3d pose estimation. In: Thirty-Second AAAI Conference on Artificial Intelligence. (2018)
17. Kipf, T.N., Welling, M.: Semi-supervised classification with graph convolutional networks. *arXiv preprint arXiv:1609.02907* (2016)
18. Atwood, J., Towsley, D.: Diffusion-convolutional neural networks. In: Proceedings of the 30th International Conference on Neural Information Processing Systems. (2016) 2001–2009



19. Levie, R., Monti, F., Bresson, X., Bronstein, M.M.: Cayleynets: Graph convolutional neural networks with complex rational spectral filters. *IEEE Transactions on Signal Processing* **67** (2018) 97–109
20. Rayat Intiaz Hossain, M., Little, J.J.: Exploiting temporal information for 3d human pose estimation. In: *Proceedings of the European Conference on Computer Vision (ECCV)*. (2018) 68–84
21. Pavlo, D., Feichtenhofer, C., Grangier, D., Auli, M.: 3d human pose estimation in video with temporal convolutions and semi-supervised training. In: *Proceedings of the IEEE Conference on Computer Vision and Pattern Recognition*. (2019) 7753–7762
22. Cai, Y., Ge, L., Liu, J., Cai, J., Cham, T.J., Yuan, J., Thalmann, N.M.: Exploiting spatial-temporal relationships for 3d pose estimation via graph convolutional networks. In: *Proceedings of the IEEE International Conference on Computer Vision*. (2019) 2272–2281
23. Isakov, K., Burkov, E., Lempitsky, V., Malkov, Y.: Learnable triangulation of human pose. In: *Proceedings of the IEEE International Conference on Computer Vision*. (2019) 7718–7727
24. Rhodin, H., Spörri, J., Katircioglu, I., Constantin, V., Meyer, F., Müller, E., Salzmann, M., Fua, P.: Learning monocular 3d human pose estimation from multi-view images. In: *Proceedings of the IEEE Conference on Computer Vision and Pattern Recognition*. (2018) 8437–8446
25. Shi, L., Zhang, Y., Cheng, J., Lu, H.: Two-stream adaptive graph convolutional networks for skeleton-based action recognition. In: *Proceedings of the IEEE Conference on Computer Vision and Pattern Recognition*. (2019) 12026–12035
26. Hamilton, W., Ying, Z., Leskovec, J.: Inductive representation learning on large graphs. In: *Advances in neural information processing systems*. (2017) 1024–1034
27. Wang, L., Chen, Y., Guo, Z., Qian, K., Lin, M., Li, H., Ren, J.S.: Generalizing monocular 3d human pose estimation in the wild. In: *Proceedings of the IEEE International Conference on Computer Vision Workshops*. (2019) 0–0
28. Chen, X., Lin, K.Y., Liu, W., Qian, C., Lin, L.: Weakly-supervised discovery of geometry-aware representation for 3d human pose estimation. In: *Proceedings of the IEEE Conference on Computer Vision and Pattern Recognition*. (2019) 10895–10904
29. Lee, K., Lee, I., Lee, S.: Propagating lstm: 3d pose estimation based on joint interdependency. In: *Proceedings of the European Conference on Computer Vision (ECCV)*. (2018) 119–135
30. Cheng, Y., Yang, B., Wang, B., Yan, W., Tan, R.T.: Occlusion-aware networks for 3d human pose estimation in video. In: *Proceedings of the IEEE International Conference on Computer Vision*. (2019) 723–732
31. Lin, M., Lin, L., Liang, X., Wang, K., Cheng, H.: Recurrent 3d pose sequence machines. In: *Proceedings of the IEEE Conference on Computer Vision and Pattern Recognition*. (2017) 810–819
32. Bruna, J., Zaremba, W., Szlam, A., LeCun, Y.: Spectral networks and locally connected networks on graphs. *arXiv preprint arXiv:1312.6203* (2013)
33. Defferrard, M., Bresson, X., Vandergheynst, P.: Convolutional neural networks on graphs with fast localized spectral filtering. In: *Advances in neural information processing systems*. (2016) 3844–3852
34. Duvenaud, D.K., Maclaurin, D., Iparraguirre, J., Bombarell, R., Hirzel, T., Aspuru-Guzik, A., Adams, R.P.: Convolutional networks on graphs for learning molecular fingerprints. In: *Advances in neural information processing systems*. (2015) 2224–2232

35. Monti, F., Boscaini, D., Masci, J., Rodola, E., Svoboda, J., Bronstein, M.M.: Geometric deep learning on graphs and manifolds using mixture model cnns. In: Proceedings of the IEEE Conference on Computer Vision and Pattern Recognition. (2017) 5115–5124
36. Veličković, P., Cucurull, G., Casanova, A., Romero, A., Lio, P., Bengio, Y.: Graph attention networks. arXiv preprint arXiv:1710.10903 (2017)
37. Ioffe, S., Szegedy, C.: Batch normalization: Accelerating deep network training by reducing internal covariate shift. arXiv preprint arXiv:1502.03167 (2015)
38. Srivastava, N., Hinton, G., Krizhevsky, A., Sutskever, I., Salakhutdinov, R.: Dropout: a simple way to prevent neural networks from overfitting. The journal of machine learning research **15** (2014) 1929–1958
39. Liu, J., Ding, H., Shahroudy, A., Duan, L.Y., Jiang, X., Wang, G., Chichung, A.K.: Feature boosting network for 3d pose estimation. IEEE transactions on pattern analysis and machine intelligence (2019)
40. Nair, V., Hinton, G.E.: Rectified linear units improve restricted boltzmann machines. In: Proceedings of the 27th international conference on machine learning (ICML-10). (2010) 807–814
41. He, K., Gkioxari, G., Dollár, P., Girshick, R.: Mask r-cnn. In: Proceedings of the IEEE international conference on computer vision. (2017) 2961–2969
42. Chen, Y., Wang, Z., Peng, Y., Zhang, Z., Yu, G., Sun, J.: Cascaded pyramid network for multi-person pose estimation. In: Proceedings of the IEEE conference on computer vision and pattern recognition. (2018) 7103–7112

## Appendix A. Supplementary Material

This supplementary material provides additional experiments to illustrate the effectiveness of our method. First, we adopt varying frame rates to validate the robustness of the proposed model. Second, we carefully analyze global attention skeleton  $B_k$  and adaptive matrix  $C_k$  through visualization to facilitate deeper understanding the construction of spatial configuration among joints.

### A.1. Varying Video Frame Rates Evaluation

In this experiment, our purpose is to assess the effect of our model on varying frame rates, which can confirm the robustness in fast and slow-motion scenes. Table 5 shows that our model (under 9 receptive fields) obtain the lowest error about 10 FPS on Human3.6M under both protocols. The reason for the poor performance at high frame rates (low motion scenes) is possible that there is an amount of redundant information among adjacent frames, which will affect encoding diverse global semantics. As for low frame rates, the large motion is harmful to exploiting the temporal consistency. Even so, as shown in the table, the performance of our model remains stable for varying frame rates.

**Table 5.** MPJPE performance when varying frames per second (FPS) from 50 FPS to 1FPS on Human3.6M under protocols 1 and 2. 10 FPS achieves the highest performance for both protocols.

FPS	50	25	10	5	2	1
Protocol #1	51.4	50.6	<b>49.0</b>	49.3	49.3	51.5
Protocol #2	39.0	38.2	<b>37.4</b>	37.6	38.4	40.3

### A.2. Global Attention Visualization

To further understand the construction of global semantics among joints, we visual our model’s global weighted matrices  $B_k$ . Weight matrices contain the average result across from multi-head attention in Eq. 3 (under 27 receptive fields). Fig. 7 is a visualization of global weighted matrix represented by skeleton graph, where the circle mass indicates the strength of the relationship between the current joint and the right ankle marked red circles in the figure.

The first-layer skeleton graph shows that there is a weak strength relationship between the right ankle and other joints. the second-layer skeleton graph shows that the relationship is mainly from the upper body, while the third-layer skeleton graph shows that the relationship is mainly from the lower body. This evaluates our hypothesis that global attention can build distal relationships and form effective constraints among joints to reconstruct valid 3D poses.

### A.3. Global Adaptive Matrices Visualization

To better understand the construction of global relationships among joints, we also visualized the global adaptive matrix  $C_k$  of each graph attention block. We

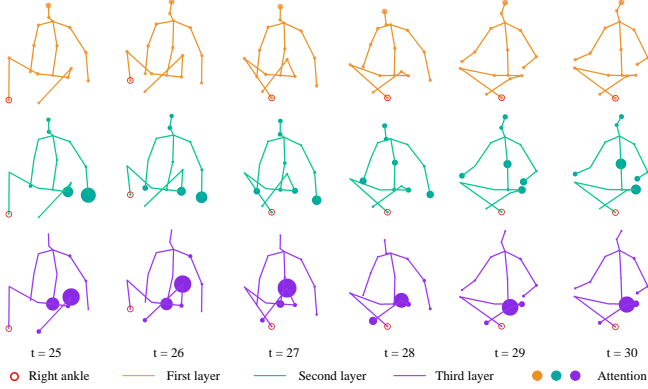


**Fig. 7.** Global attention weight matrix visualization. The right ankle is set as the visualized joint. Three colored layers represent three different attention layers advancing from top to bottom. Columns indicate time frames. Circle mass indicates the relationship strength between the current and the visualized joint.

perform the experiment on our 27 receptive field model, which consists of 3 graph attention blocks. Weight matrices contain the average result across from multi-head attention in Eq. 3. The visualization is shown in Fig. 8. We observe that the adaptive matrix can effectively model the spatial configuration for each joint, not just local connections. The weighted value of matrices is from  $-0.65$  to  $0.25$ , and no extreme values have been learned, which illustrates the rationality of the adaptive matrix. As for the negative value in the matrix, we speculate that this suppresses the strength of relationships between the corresponding joints learned by  $B_k$ , while the positive value helps to enhance the strength. But it is worth noting that most of these values are very small and do not play a decisive role compared to  $B_k$ .

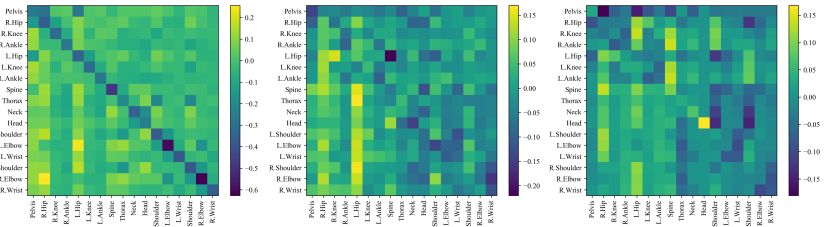


**Fig. 8.** Visualization of global adaptive matrices across 3 attention blocks. Each global adaptive matrix learns unique weights among joints. The color gradient represents the strength of relationships between joints.